Monte Carlo Simulation of the Radiation Field in a Reticulated Foam Photocatalytic Reactor

Rajnish Changrani and Gregory B. Raupp
Dept. of Chemical, Bio and Materials Engineering, Arizona State University, Tempe, AZ 85287

The 3-D polychromatic radiation field for an annular packed-bed photocatalytic reactor using alumina reticulated foams as a monolithic catalyst support was simulated using Monte Carlo methodology. Two distinct methods were used for simulating photon transport: (1) a ''spatial'' approach that tracks the flight of a photon in a predetermined reticulate structure; (2) a ''temporal'' approach that generates the random porous structure of the reticulate as the photon flies into it. The two approaches yield almost identical results, although the temporal approach is far more efficient computationally. Simulations for the integral axially-averaged radial ultraviolet (UV) light profiles agree closely with experimental measurements for titania-coated 10, 20 and 30 PPI alumina reticulates and near UV lamps. The simulations reveal that the local volumetric rate of energy absorption (LVREA) in the reticulate and the magnitude of the LVREA gradient both increase with decreasing reticulate pore size.

Introduction

Increasingly strict air emission standards are creating demands for new technologies to treat trace organic contaminants in air. Traditionally, the control of volatile organic compound (VOC) emissions has been accomplished using energy intensive thermal incineration and/or regenerable adsorbents. Gas-solid photocatalytic oxidation (PCO) is an emerging technology for destruction of dilute VOCs in air that is currently under commercial development (Dibble, 1989; Dibble and Raupp, 1990, 1992; Peral and Ollis, 1992; Junio and Raupp, 1993; Raupp, 1995; Obee and Brown, 1995; Sauer and Ollis, 1996).

Despite its potential advantages, PCO has been slow to make its way into the air treatment and purification marketplace. A critical barrier that has contributed to PCO's lack of widespread commercial realization is the lack of suitable photocatalytic reactor models and design procedures (Cassano et al., 1995).

Commercial or near-commercial PCO reactor designs have evolved into two basic, inherently different configurations for distributing the catalyst: (i) channeled or honeycomb monoliths; or (ii) random, porous monolith structures. In recent publications we have developed rigorous radiation field models and fluid-flow models for the honeycomb monolith designs (Hossain and Raupp, 1998a,b,c). In the channeled monolith configuration, the geometry is well defined, allowing direct numerical solution of the governing integro-differential equations for the radiation field and differential equations for the fluid-flow field. In contrast, random, porous monolith structures significantly complicate the radiation field and fluid-flow field to the extent that direct numerical solution of the integro-differential model equations (Spadoni et al., 1978; Cassano et al., 1995) is problematic except for the simplest of geometries (such as plane slab) and somewhat unrealistic assumptions on the photon-solid interactions (Cassano et al., 1995). In tackling more complicated geometries and more rigorous models, stochastic simulation methods (such as Monte Carlo methods) are preferred over deterministic methods. Monte Carlo simulations track individual photons from their ''birth'' at the source of their ultimate ''fate'' —either absorption within the reacting network, or escape from the system by out-scattering (when photons escape the reaction system due to multiple forward scattering events).

Spadoni et al. (1978) were the first to use Monte Carlo simulation to model the radiation field in an annular photocatalytic reactor with an aqueous slurry of titania flowing in the annular space. More recently, Pasquali et al. (1996) used Monte Carlo simulations for this reactor system to calculate the local volumetric rate of energy absorption (LVREA) as a

---

Correspondence concerning this article should be addressed to G. B. Raupp.

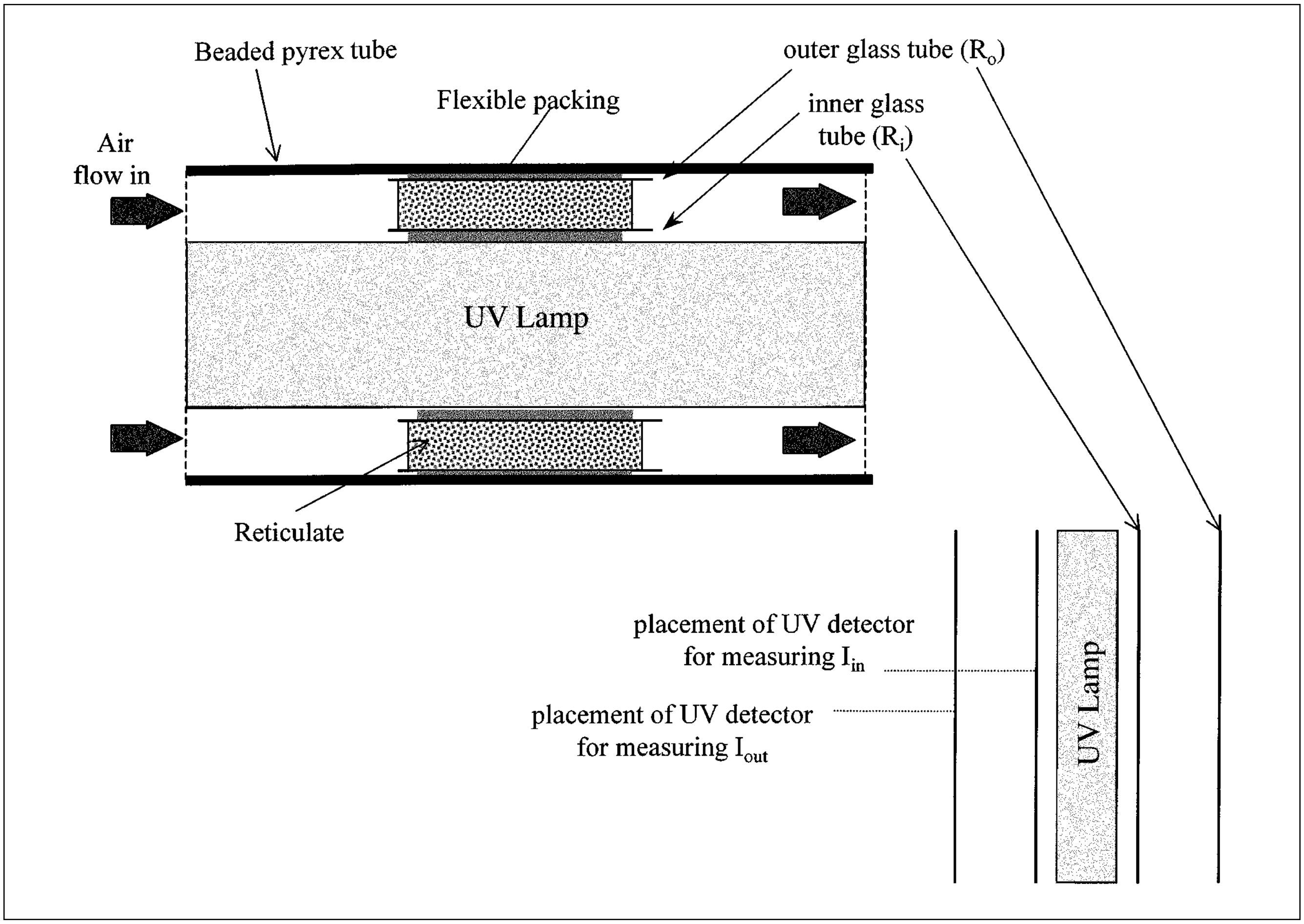

Figure 1. Bench-scale annular photocatalytic reactor showing the spatial relationship between the reticulated foam monolith and the UV lamp.

function of the following characteristics of the system: *optical thickness, scattering albedo, and phase function.* These articles have modeled a 2-D *mono*chromatic radiation field, and the lamp has been modeled as a diffusely emitting *linear* source. Although these contributions have generated a solid theoretical base for studying heterogeneous photoreactors, few validating experiments were performed, and system parameters (such as absorption and scattering coefficients) for presenting the model predictions are usually the result of estimations within realistic limits of typical values rather than physically-real corresponding to an actual system.

In this article we use Monte Carlo simulations to model a 3-D *poly*chromatic radiation field in an annular coated reticulated foam photoreactor. The lamp is modeled as a source of *finite size* with *superficial emission.* System parameters such as wavelength-dependent scattering coefficients are obtained from experimental data available in the literature, and model simulations are compared with experimental observations.

Physical System and Experimental Measurements

Figure 1 represents the bench-scale annular photocatalytic reactor. The monolithic structure that forms the catalyst support is one of three alumina reticulates (99.5% alumina) manufactured by Hi-Tech Ceramics. The reticulate consists of a ‘‘web’’like interconnecting alumina strut structure, which forms randomly-distributed near spherically-shaped pores with diameters normally distributed about a mean value. The manufacturer classifies these reticulates by pores-per-inch (PPI), a value that only roughly corresponds to the number of pores found in a linear inch of reticulate. We have conducted experiments with 10, 20, and 30 PPI reticulates; Table 1 lists the properties of these reticulated structures. Figure 2 is a digital photograph of the 10 PPI and 30 PPI reticulates.

A concentric 20-W low-pressure mercury lamp (GE F20T12-BLB) irradiates the reticulate in the annular space. The reticulate is sized so that it is irradiated largely by the middle third of the lamp where the UV intensity is most intense and most uniform. Ultraviolet light fluxes at the reactor inner wall and the outer wall (see Figure 1) in the 310–400

Table 1. Reticulate Ceramic Properties

Pores/in.	Mean Pore Size (mm)	Surface Area (m^2/m^3)
10	1.5	2,290
20	1.0	3,400
30	0.75	4,370

SI conversion: mm = in. × 25.4.

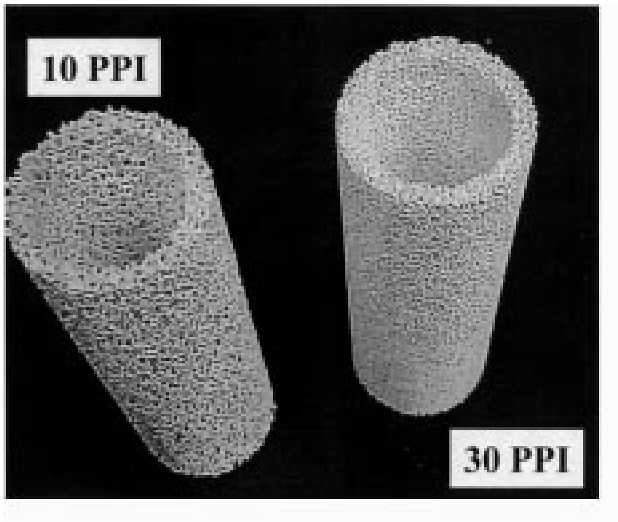

Figure 2. 10 PPI and the 30 PPI reticulates.

nm wavelength range were measured with a Minolta integrating photometer. The spectral power distribution of the fluorescent 20-W UV "black lamp" was measured with a Spectrofluoro photometer (Shimadzu RF-1501).

Ultraviolet flux measurements were conducted on uncoated reticulates and on reticulates coated with a film of TiO_2. The alumina reticulates were washcoated using a Degussa P25 slurry in distilled water. In order to study the effect of catalyst film thickness on the LVREA for a fixed reticulate configuration, the catalyst loading on the 20 PPI reticulate was increased in steps with two sequential wash coats. The catalyst film thickness for the 20 PPI reticulate with the final catalyst loading in the series of coatings and the thickness for the 30 PPI reticulate were measured using a scanning electron microscope (SEM). Figure 3 is a SEM micrograph of a strut cross-section for the 30 PPI coated reticulate. The film appears to be contiguous with moderate uniformity. On this basis, film thicknesses for which high quality SEM images could not be obtained were estimated using a simple model in which it is assumed that the known external surface area of the reticulate is uniformly coated by the catalyst thin film, and that the film porosity is 50%. Table 2 compares film thickness estimates with the available experimental measurements. The comparison shows that the simple model provides a reasonable estimate of the mean catalyst film thickness.

Model Development

Model assumptions

(1) The UV lamp is modeled as a polychromatic extended-source with superficial emission (ESSE). This model assumes a uniform emission from the surface of the lamp and its directional independence.

(2) Axial variations in the lamp emission intensity are ignored.

(3) The spectral distribution of the low-pressure mercury "blacklamp" is given by the sum of two Gaussian distributions centered about 366 and 404 nm in wavelength.

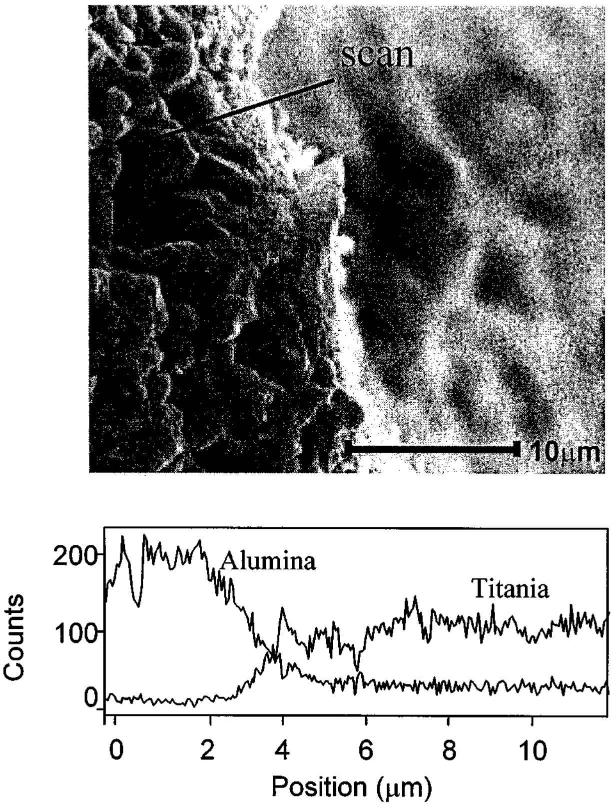

Figure 3. Scanning electron microscopy analysis of the cross-section of a strut of the 30 PPI reticulate with a catalyst loading of 0.26 g.

Top: SEM micrograph showing the thin, nanoporous titania thin film on the microporous reticulate; *bottom:* titanium and aluminum X-ray line scan along the line indicated on the micrograph.

(4) Photons that encounter the lamp after undergoing multiple-scattering events are absorbed by the lamp, resulting in emission of a new photon.

(5) Light interaction with the fluid phase is negligible.

(6) Scattering by the solid phase is assumed to be elastic (energy is conserved), independent, and perfectly diffuse.

(7) The pores formed by the interconnecting alumina struts within each reticulate are considered to be spherical in shape. The pore-size distribution within each reticulate is modeled as a Gaussian; mean pore size and variance are obtained from the manufacturer's data.

Table 2. Catalyst Film Thickness: Calculated and Measured

Reticulate (PPI)	Catalyst Loading (g)	Film Thickness Calculated (μm)	Film Thickness Measured (μm)
10	0.19	1.9	—
20	0.21	2.0	—
20	0.34	3.2	—
20	0.53	5.1	5.0
30	0.26	2.5	3.0

(8) The extinction coefficient of TiO_2 is assumed to be 0.3 μm^{-1}. This value is based on data that indicate that 99% of the incident UV is captured in the first 15 μm of a titania powder bed (Formenti et al., 1971).

(9) Optical thin film properties (absorbance and reflectance) are independent of light incidence angle and also are independent of catalyst film thickness.

Structural considerations and Monte Carlo approaches

For simulation of the radiation field in the random, porous reticulate structure, two different approaches have been employed. In the first "spatial" approach (Method A), the random pore structure of the reticulate is generated by using Monte Carlo methods to randomly choose pore locations and pore diameters to match the reticulate parameters summarized in Table 1. Physically, the reticulate structure is composed of interconnecting alumina struts forming a random distribution of interconnecting pores; to model this structure, we employed randomly generated spherical pores overlapping in space. The random number generator *ran1* (Press et al., 1996) used to randomly distribute the pores in the 3-D reticulate incorporates a built-in algorithm to remove any low-order serial correlation. This porous structure is stored in memory. The photons emitted randomly from the lamp then fly into this fixed random structure, where they are tracked analytically to determine locations for solid scattering. Because the flight length decision is made deterministically based on the entire reticulate structure, this approach is spatial in nature.

In the second "temporal" approach (Method B), the reticulate pore structure is generated as the photon flies into it. For a photon traveling a given path through a given pore, the flight length decision is made stochastically and is based on the reticulate voidage. Specifically, the current flight length of the photon is determined analytically based on information (pore center coordinates and radius) about the pore randomly generated at the "current" location of the photon, and information about the pore at the "previous" location of the photon. Because each photon effectively "sees" a different random structure, this approach is temporal in nature.

As expected, the computer code employing Method A (spatial approach) requires significantly more memory than the corresponding code employing Method B (temporal approach), and the time required for program execution for 10^5 photons is approximately 50 h on a desktop machine (Pentium II 266 MHz). In contrast, the time required for Method B program execution for 10^5 photons is 0.05 h on the same machine.

Geometric considerations

To develop a mathematical model or simulation of the 3-D radiation field for an annular reactor configuration, one could employ a cylindrical coordinate system using two spatial variables (r, z) and two directional variables (θ, ϕ). Alternatively, one could use the (x, y, z) Cartesian coordinate system. Figure 4 shows the spatial relationship between the two candidate coordinate systems for coordinate systems centered arbitrarily at a photon scattering point A. Even though the problem of interest possesses cylindrical symmetry, there are computational advantages in employing Cartesian coordinates for simulation of individual photon flight paths. These advantages arise because a particle's direction of flight in Cartesian coordinates is uniquely specified by the direction cosines (e_x, e_y, e_z) with respect to the x, y, and z axes, respectively. The new position B of a photon after traveling a distance λ from point A (see Figure 4) is then simply determined by

$$x_B = x_A + e_x \lambda \tag{1}$$

$$y_B = y_A + e_y \lambda \tag{2}$$

$$z_B = z_A + e_z \lambda \tag{3}$$

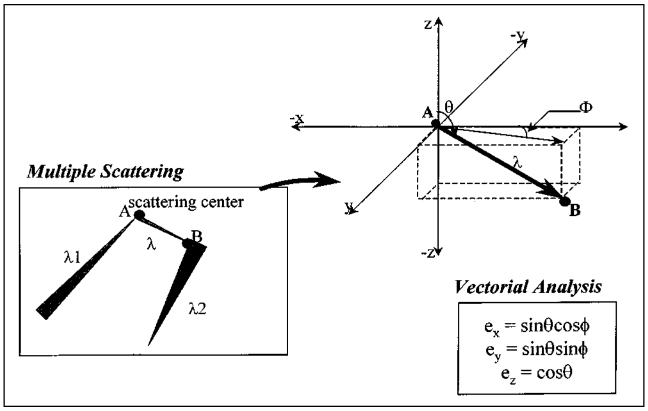

Figure 4. Explanation of the vectorial analysis of a multiple scattering event at an arbitrary point in the reticulate.

Monte Carlo methodology

Monte Carlo simulations use random sampling to simulate the solution of a physical or mathematical problem. In this subsection we briefly describe the sequence of events that are simulated for the present radiation field problem, and state the probability distributions used to describe these events. Figure 5a details the overall Monte Carlo simulation algorithm. In both the "spatial" as well as the "temporal" approaches employed in the Monte Carlo simulations, there are essentially three parts to the problem. The first part called *generation* simulates photon emission from the UV source, the second part called *transport* simulates the random flight length of the photon in the reticulate structure, and the third part called *interaction* simulates photon-solid interaction. Figure 5b details the algorithm for the interaction submodel.

(1) *Photon Generation.* The photon generation submodel uses three random numbers to simulate photon emission from the UV source. The following explains the logic underlying the generation of these three random numbers.

- Choice of the Photon Wavelength (energy): The bimodal spectral distribution characteristic of the low-pressure mercury lamp used in our experiments is accurately simulated by two overlapping Gaussian distributions. The wavelength of the photon is determined using a random number sampled from either of these two Gaussian distributions. An inde-

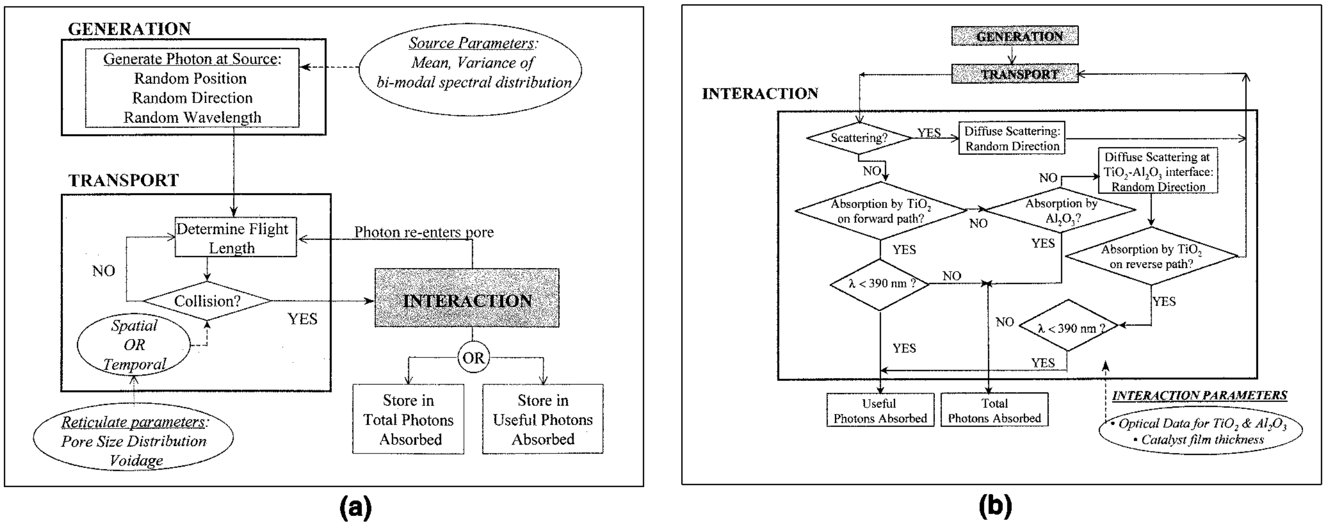

Figure 5. Structure of the Monte Carlo simulation.

(a) Overall structure showing the interrelationship of the three main submodels; (b) structure of the photon-solid interaction submodel.

pendent simulation to model the spectral distribution of the UV lamp was employed to determine the model parameters including the sampling ratio between the distributions (see the subsection on model parameters).

- Choice of the Photon Emission Point: The emission point on the surface of the lamp is determined by using two random numbers. One random number sets the point along the length of the lamp $U(-L/2, L/2)$ at which the photon is emitted. The other random number fixes the point along the circumference of the lamp $U(0, 2\pi)$ at which the photon is emitted.
- Choice of the Photon Direction of Flight: The direction of photon flight is determined by two angles—the longitudinal angle θ_e and the equatorial angle ϕ_e. These angles are determined using two random numbers distributed uniformly on $(0, \pi)$ and $(-\pi/2, \pi/2)$, respectively.

(2) *Photon Transport.* The photon transport submodel evaluates the flight length of the photon within a given pore, and determines whether or not the photon flies into an adjacent pore or instead strikes the present pore wall. The following explains the underlying logic in the evaluation of the total flight length.

- Evaluation of the Photon Flight Length in the Current Pore: The pore radii within each reticulate follow a Gaussian distribution. Therefore, the flight length of the photon between each interaction with the reticulate will be different depending upon both the dimension of the pore it encounters, and its direction of flight. However, for known state variables defining the pore (that is, the pore radius and the coordinates of the pore center) and the angles defining the direction of flight of the photon, the flight length of the photon within that pore can be calculated in a deterministic manner using elementary geometry.
- Evaluating if Photon Flies into an Adjacent Pore: The two methodologies employed in the Monte Carlo simulations differ in the mechanism used to determine whether a photon flies into an adjacent pore or instead strikes a pore wall. In the "spatial" approach the details of the entire reticulate (that is, the center coordinates and radius for each pore) are stored in memory. At any given point in the flight of the photon, the entire reticulate is spanned to check whether the photon is within any of the pores. If the photon does not happen to be in any of the tens of thousands of pores, then we conclude an interaction with the solid boundary has occurred. In the "temporal" approach the occurrence of an interaction is determined probabilistically, by recognizing the fact that the probability a photon will not interact with the solid boundary is equal to the voidage of the reticulate.

(3) *Photon-Solid Interaction.* At each interaction with the reticulate, the photon can be scattered (diffusely reflected), transmitted, or absorbed. Diffuse scattering is modeled by generating two uniformly distributed random numbers—$\theta(0,\pi)$ and $\phi(0,2\pi)$—that represent the random new direction of photon flight. Figure 5b summarizes the algorithm employed to determine the nature of the photon-solid interaction. A photon that does not scatter could be absorbed by the catalyst film on the forward path (that is, from the pore to the catalyst-support interface). However, if the photon is not absorbed on the forward path, then it could be scattered at the catalyst-support interface or be absorbed by the support. If the photon is scattered at the catalyst-support interface, then it may be absorbed upon traversing the reverse path. The probability of photon absorption on either the forward path or the backward path is governed by the catalyst film thickness and the extinction coefficient of the film. Photons that are not absorbed by the catalyst on the forward or the reverse path, and are not absorbed by the support, are transmitted and, therefore, re-enter the pore with a new direction. The program control then returns to the transport submodel.

The fate of the photon at a given interaction event is determined by generating a random number ξ uniformly distributed on $(0,1)$. Let κ_υ be the film thickness-dependent absorption coefficient as governed by Beer's Law and σ_υ the

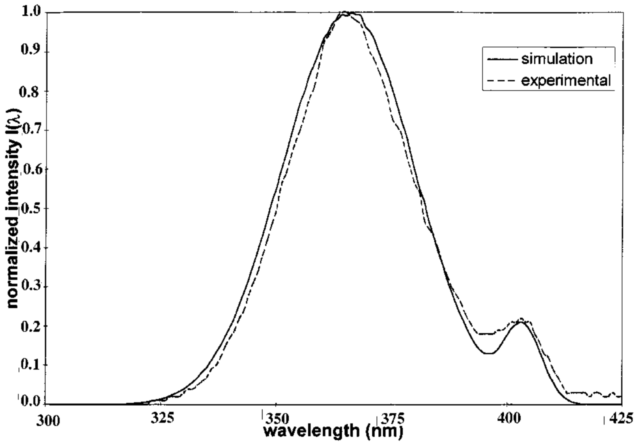

Figure 6. Spectral distribution of the UV source: comparison of experimental data (---) with Monte Carlo simulation (——).

scattering coefficient. Then, the following relationships define the nature of the photon-solid interaction event

$\xi \le \kappa_v$	absorption occurs
$\kappa_v < \xi \le \kappa_v + \sigma_v$	scattering occurs
$\kappa_v + \sigma_v < \xi$	transmission occurs

Model parameters

The parameters associated with simulation of the UV source are the mean and the variance of the two overlapping Gaussian distributions and the sampling ratio between the two Gaussians. Figure 6 compares the experimental UV source spectral distribution with a Monte Carlo simulation employing 10^6 photons. An accurate description of the source was found by employing a mean of 366 nm and variance of 13 nm^2 for the primary Gaussian distribution, and a mean of 404 nm and variance of 4 nm^2 for the secondary Gaussian, as well as by sampling the primary distribution 19 times more often than the secondary distribution.

The parameters associated with photon flight length are essentially those defining the reticulate structure including: (i) mean pore radii; (ii) variance of the pore-size distribution; (iii) voidage of the reticulate structure. Table 3 summarizes the model parameters required for generating the reticulate structure. The voidage for each reticulate was calculated using the following empirical relationship (Obee, 1996)

$$\epsilon = (d \cdot a_v)/4.0 \qquad (4)$$

where d is the mean pore diameter and a_v is the BET external surface area pore unit volume of the reticulate. With the exception of reticulate voidage, all reticulate model parameters were obtained directly from the manufacturer's data and were used without adjustment. In practice, we found that a modest adjustment to the estimated reticulate voidage provided a better fit to the light intensity data.

Table 3. Model Parameters for Generation of Reticulate Structure

Reticulate (PPI)	Mean Pore Dia.* (mm)	Variance* (mm^2)	a_v^* (cm^2/cm^3)	Voidage Calc. From Eq. 4	Voidage Used in Simul.
10	1.5	0.18	22.9	0.87	0.87
20	1.0	0.15	34.0	0.85	0.87
30	0.75	0.12	43.7	0.82	0.83

*Mean pore diameter, variance and a_v obtained from manufacturer.

The parameters associated with photon-solid interaction are: (i) wavelength-dependent scattering coefficients of alumina and titania; (ii) extinction coefficient of titania; (iii) titania catalyst film thickness. Table 4 summarizes information on the model parameters for photon transport and absorption; in all cases, the model parameters were obtained from direct measurements available in the literature.

Table 4. Model Parameters for Photon Transport and Absorption

Parameter	Source
Wavelength-Dependent Scattering Coeff.	
TiO_2	Brucato (1998)
Al_2O_3	Loddo et al. (1998)
Catalyst Film Thickness	SEM measurements and thickness calculations (Table 2)
Extinction Coefficient of TiO_2	Formenti et al. (1971)

Results and Discussion

Figure 6 compares the experimentally measured spectral lamp distribution with that obtained from a Monte Carlo simulation of the spectral distribution. This comparison demonstrates that the simulation provides an excellent representation of the distribution of wavelengths emitted from the lamp. The only significant mismatch between simulation and experiment occurs for wavelengths above about 390 nm. In light of the fact that the energy of these photons is below that of the 3.2 eV titania bandgap (Hoffmann et al., 1995) this mismatch should not have a deleterious impact on model-predicted LVREAs.

The predicted dimensionless z-averaged radial photon transmitted and photon absorbed intensity profiles for the *uncoated* 10 PPI reticulate using the two different approaches to determine photon flight length (Method A and Method B) are compared in Figure 7. The two approaches give almost identical results for both the photons transmitted and the photons that are absorbed. This comparison, as well as similar comparisons for other configurations and conditions, validates the simpler virtual approach (Method B). The results to be presented subsequently in this article were therefore obtained using the more computationally efficient Method B.

Figure 8a shows the z-averaged radial dimensionless UV profiles for transmitted and absorbed photons in the 10 PPI reticulate with a catalyst loading of 0.19 g. The dimensionless transmitted UV flux at the outer wall is 0.2, which is in close

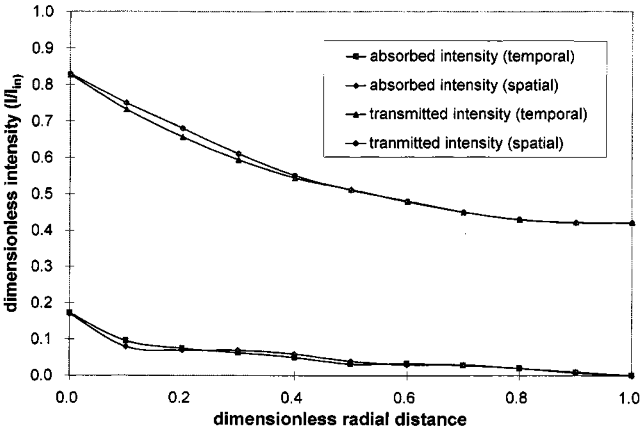

Figure 7. Comparison of the simulated dimensionless radial UV intensity profiles (both transmitted and absorbed) for the uncoated 10 PPI reticulate using the spatial simulation approach and the temporal simulation approach.

agreement with the experimental observation of 0.21. Figure 8b is the corresponding LVREA profile for a mean incident UV intensity of 3.9 mW/cm^2. Figure 9a is the *z*-averaged radial dimensionless UV profiles for the 30 PPI reticulate with a catalyst loading of 0.26 g. The dimensionless transmitted UV flux at the outer wall is 0.03, which once again is in close agreement with the experimentally observed value of 0.01. Figure 9b is the corresponding LVREA profile for a mean incident UV intensity of 3.8 mW/cm^2. In Figures 8a and 9a, the curve for the total photons absorbed represents those photons absorbed by the titania catalyst film *and* the alumina reticulate, and the curve for the useful photons absorbed represents photons with a wavelength lower than 390 nm that are absorbed by the titania catalyst film.

There is an apparent anomaly in the predictions represented in Figure 9a at dimensionless radial positions close to zero. In a differential annulus between dimensionless radii 0 and about 0.05, it appears that the absorbed intensity fraction is larger than the transmitted fraction—implying that the UV energy absorbed in this spatial increment is greater than the UV energy reaching it. This anomaly arises because of the simulation strategy that describes the reticulate volume with 10 "bins" along the radial direction. Thus, the only points along the curves in Figure 9a that have physical meaning are those at dimensionless radii of 0, 0.1, 0.2, and so on. The physical properties of the reticulate do not warrant simulations on a small radial scale, since the mean pore size over the three different reticulated structures is approximately 1 mm and the average number of solid "struts" (that is, points where photon-solid interaction could occur) in the annular width of the reactor is only 10.

The simulations reveal that the useful LVREA in the portion of the reticulate near the lamp (small dimensionless radial distance) is approximately a factor of two higher for the 30 PPI reticulate relative to that for the 10 PPI reticulate. However, the LVREA dies away faster with radial distance into the 30 PPI reticulate, leading to lower LVREA values for dimensionless radial distances greater than about 0.5. Overall the 30 PPI reticulate captures a higher fraction of the incident UV light energy, but at a cost of a greater LVREA gradient and a resulting "dark" portion of the reticulate near the outer radius of the reactor. This result highlights the key tradeoff to be optimized in choice of reticulate pore size and annular photoreactor radii.

Figure 10 shows the effect of catalyst loading on the amount of incident energy captured by the 20 PPI reticulate. Increasing the catalyst loading from 0.21 g to 0.34 g, corresponding to an increase in the estimated average titania film thickness from 2.0 to 3.2 μm, increases the LVREA by only about 4% to 5%. A further increase in loading to 0.53 g, corresponding to an estimated film thickness of 5.1 μm, increases the LVREA by only about less than 1%. These LVREA trends suggest that the best reactor performance for a given reticulate will be obtained when the titania catalyst coating is sufficiently thick to capture any UV photons impinging at that point. Physically, this critical thickness is desired because a substantial fraction of the light transmitting through the tita-

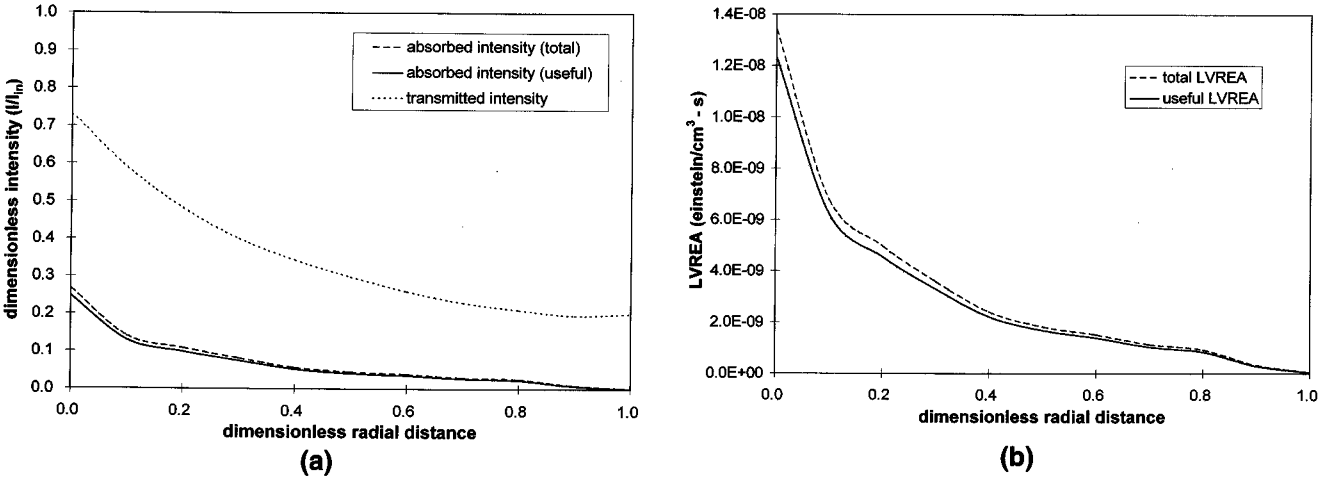

Figure 8. Axial-averaged radial profiles for the 10 PPI reticulate with a catalyst loading of 0.19 g.

(a) Dimensionless transmitted and absorbed intensity; (b) local volumetric rate of energy absorption (LVREA).

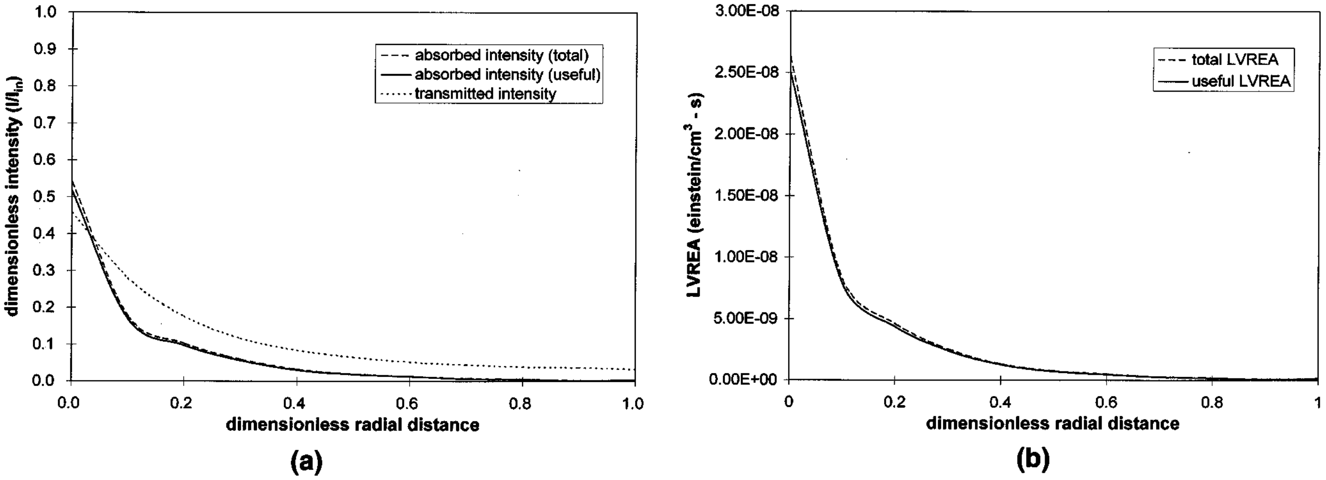

Figure 9. Axial-averaged radial profiles for the 30 PPI reticulate with a catalyst loading of 0.26 g.

(a) Dimensionless transmitted and absorbed intensity; (b) local volumetric rate of energy absorption (LVREA).

nia thin film will be absorbed by the photocatalytically-inert alumina support. This expectation is consistent with our previously published phenomenological study of isopropanol PCO (Changrani and Raupp, 1998) employing the annular photocatalytic reactor modeled in the present work. Specifically, reactor performance increased modestly with the first catalyst loading increase from 0.21 g to 0.34 g, but displayed no substantial performance improvement for a further catalyst loading increase to 0.53 g.

Because experimental measurements of catalyst film thickness are available for only two catalyst loadings, we carried out a model sensitivity analysis on the influence of catalyst film thickness. This analysis revealed a relative insensitivity of model predictions for UV fraction absorbed on catalyst film thickness. For example, doubling catalyst thickness from 1 to 2 μm increases the UV fraction absorbed by only about 6%. We therefore conclude that this parameter is not critical to the overall simulation results, and that the uncertainty on film thickness values translates into only a small uncertainty on model outcomes.

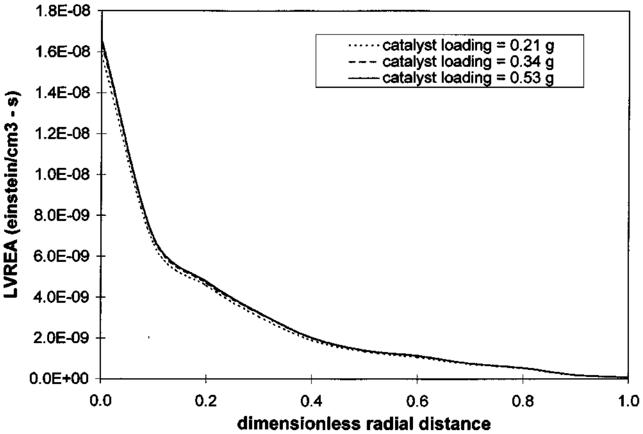

Figure 10. Effect of catalyst loading on the LVREA radial profile for the 20 PPI reticulate.

Table 5 shows the experimental observations for the fraction of UV energy absorbed with those given by Monte Carlo simulations for all three reticulates, including the 20 PPI reticulate with three catalyst loadings. This direct comparison demonstrates that simulator predictions are uniformly in good agreement with the experimental observations. Recall that this match is achieved with the benefit of only a *slight* adjustment of a *single* parameter related to the randomness of the reticulate structure—the reticulate voidage. In light of the fact that the voidage values were calculated using a semiempirical relation (Eq. 4) that is only rigorously correct for a reticulate containing monosized pores, it is not surprising that this parameter required some adjustment.

To evaluate the predictive capability of the model, a sensitivity analysis on the voidage model parameter was performed; the results of this analysis are summarized visually in Figure 11 for the 10 PPI reticulate. The analysis reveals that model results are particularly sensitive to this parameter with increasing sensitivity at higher absolute voidage values. Quantitatively, a 1% increase in assumed voidage at a voidage value of 0.87 leads to a 2.5% relative decrease in fraction UV absorbed. At a voidage of 0.89, this sensitivity increases to −3.5%.

With confidence that the model captures the underlying physics of photon transport and absorption in reticulated

Table 5. Predicted and Measured Fraction UV Absorbed

Reticulate (PPI)	Catalyst Loading (g)	Fraction UV Absorbed (Pred.)	Fraction UV Absorbed (Exp.)
10	0	0.58	0.58
	0.19	0.80	0.79
20	0	0.67	0.66
	0.21	0.90	0.90
	0.34	0.93	0.94
	0.53	0.94	0.95
30	0	0.73	0.72
	0.26	0.97	0.99

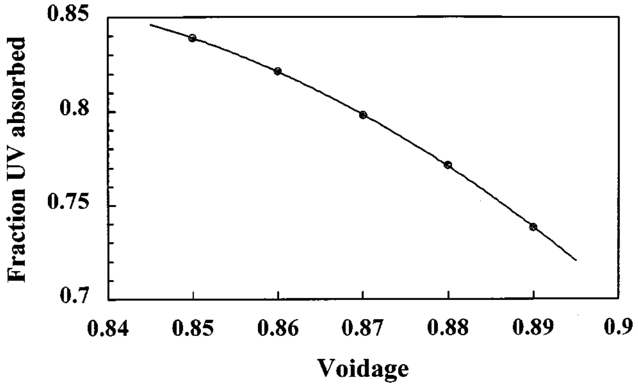

Figure 11. Model parameter sensitivity analysis.

Fraction UV absorbed vs. reticulate voidage for the 10 PPI reticulate.

structures, albeit with a single model parameter adjustment, we now employ model predictions to gain insight into the annular and axial LVREA profiles within the reticulate. Figure 12 is the z-averaged angular dimensionless profile of the LVREA for the 30 PPI reticulate at the inner wall of the photoreactor ($R = 0$), and midway through the reactor ($R = 0.5$). The angular symmetry of these angular profiles shows that the 3-D radiation field may be collapsed onto a 2-D r-z plane for photocatalytic reactor modeling purposes without considerable loss in accuracy.

Figure 13 is the r-averaged axial dimensionless profile for the photons absorbed within the coated 30 PPI reticulate. The average number of photons absorbed is almost uniform in the middle region portion of the reticulate ($0.50 < Z < 0.80$). However, towards the end of the reticulate ($Z > 0.9$), the average number of photons absorbed drops significantly. This decrease is in line with the fact that at the entrance ($Z \rightarrow 0$ not shown in the figure), as well as at the exit ($Z \rightarrow 1$), the probability of a photon escaping from either face ($Z = 0$ or $Z = 1$) begins to increase. Recall that this model assumed that the incident photon intensity was independent of axial distance. In reality, lamps exhibit a substantial axial emission nonuniformity, and, hence, the gradient suggested in Figure 12 would likely be more severe in practice.

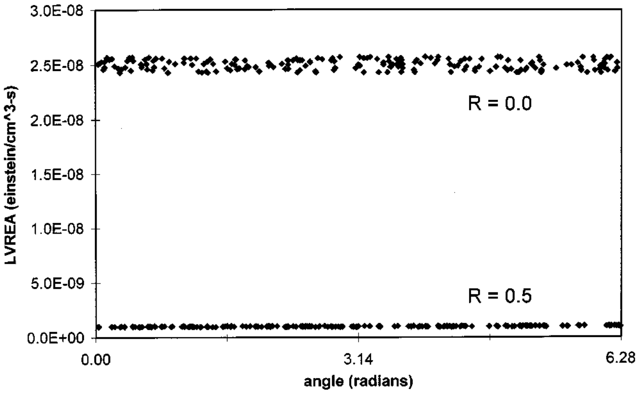

Figure 12. Simulated angular profiles for the LVREA for the 30 PPI reticulate with a catalyst loading of 0.26 g.

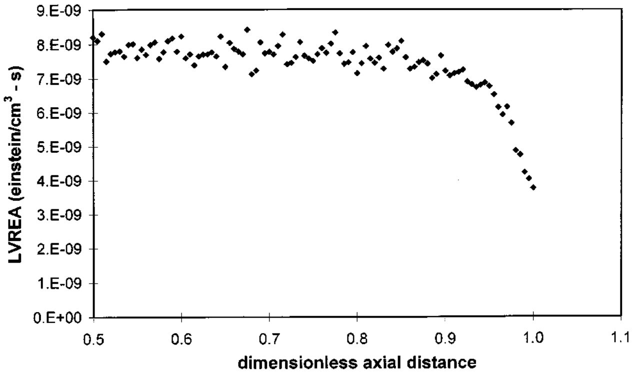

Figure 13. Simulated axial profile of the LVREA for the 30 PPI reticulate with a catalyst loading of 0.26 g.

Conclusions

We have employed Monte Carlo methodology to simulate the 3-D polychromatic UV radiation field in an annular heterogeneous gas-solid photocatalytic reactor with alumina reticulated foams as a monolithic catalyst support structure. Within the limitations of the model assumptions, the UV intensity profiles are determined by the spectral power distribution of the light source, the pore-size distribution of the reticulate, the reticulate voidage, the average titania catalyst film thickness, the extinction coefficient of the catalyst film, and the wavelength-dependent optical properties of the catalyst film and underlying alumina support. Experimental measurements of UV flux at the outer wall of the reactor are in close agreement with model simulations. This validated model can now be used confidently as the radiation field submodel in a full heterogeneous convection-reaction model for a fixed-bed gas-solid photocatalytic reactor to explore the PCO process capabilities and inherent limitations of reticulated foam-based reactor configurations.

Acknowledgments

The authors gratefully acknowledge the financial support of the U.S. EPA for the experimental portion of this work. We also thank Dr. Truett Sweeting of High Tech Ceramics for fabricating the custom reticulates to our specifications. Finally, we are grateful to Dr. Tom Taylor of the Mathematics Department at ASU for valuable advice concerning the Monte Carlo simulations.

Literature Cited

Brucato, A., "Wavelength Dependent Reflectivities for TiO_2 Films," personal communication (1998).

Cassano, A. E., C. A. Martin, R. J. Brandi, and O. M. Alfano, "Photoreactor Analysis and Design: Fundamentals and Applications," *Ind. Eng. Chem. Res.*, **34**, 2155 (1995).

Changrani, R., and G. B. Raupp, "Performance Evaluation of a Titania-Coated Reticulated Foam Photocatalytic Oxidation Reactor," *J. Adv. Oxid. Technol.*, **3**, 277 (1998).

Dibble, L. A., "Gas-Solid Heterogeneous Photocatalytic Oxidation of Trichloroethylene by Near UV-Irradiated Titanium Dioxide," PhD Diss., Arizona State University, Tempe, AZ (1989).

Dibble, L. A., and G. B. Raupp, ''Kinetics of the Gas-Solid Heterogeneous Photocatalytic Oxidation of Trichloroethylene over Near UV-Irradiated Titanium Dioxide,'' *Catal. Lett.*, **4**, 345 (1990).

Dibble, L. A., and G. B. Raupp, ''Fluidized-Bed Photocatalytic Oxidation of Trichloroethylene in Contaminated Air Streams,'' *Environ. Sci. Technol.*, **26**, 492 (1992).

Formenti, M., F. Juillet, P. Meriadeau, and S. J. Teichner, ''Heterogeneous Photocatalysis for Partial Oxidation of Paraffins,'' *Chem. Technol.*, **1**, 680 (1971).

Hoffmann, M. R., S. T. Martin, W. Choi, and D. W. Bahnemann, ''Environmental Applications of Semiconductor Photocatalysis,'' *Chem. Rev.*, **95**, 69 (1995).

Hossain, Md. M., and G. B. Raupp, ''Radiation Field Modeling in a Photocatalytic Monolith Reactor,'' *Chem. Eng. Sci.*, **53**, 3771 (1998a).

Hossain, Md. M., and G. B. Raupp, ''Polychromatic Radiation Field Model for a Honeycomb Monolith Photocatalytic Reactor,'' *Chem. Eng. Sci.*, in press (1998b).

Hossain, Md. M., and G. B. Raupp, ''Modeling of a Photocatalytic Honeycombed Monolith Reactor for Air Purification Processes,'' *J. Adv. Oxid. Technol.*, **3**, 285 (1998c).

Junio, C. T., and G. B. Raupp, ''Photocatalytic Oxidation of Oxygenated Air Toxics,'' *Appl. Surf. Sci.*, **72**, 321 (1993).

Loddo, V., G. Marci, L. Palmisano, and A. Sclafani, ''Preparation and Characterization of Al_2O_3 Supported TiO_2 Catalysts Employed for 4-Nitrophenol Photodegradation in Aqueous Medium,'' *Matls. Chem. Phys.*, **53**, 217 (1998).

Obee, T. N., and R. T. Brown, ''TiO_2 Photocatalysis for Indoor Air Applications: Effects of Humidity and Trace Contaminant Levels on the Oxidation Rates of Formaldehyde, Toluene, and 1,3-Butadiene,'' *Environ. Sci. Technol.*, **29**, 1223 (1995).

Obee, T. N., ''Photooxidation of Sub-Parts-Per-Million Toluene and Formaldehyde Levels on Titania Glass-Plate Reactor,'' *Environ. Sci. Technol.*, **30**, 3578 (1996).

Pasquali, M., F. Santarelli, J. Porter, and P. Yue, ''Radiative Transfer in Photocatalytic Systems,'' *AIChE J.*, **42**, 532 (1996).

Peral, J., and D. F. Ollis, ''Heterogeneous Photocatalytic Oxidation of Gas-Phase Organics for Air Purification: Acetone, 1-Butanol, Butyraldehyde, Formaldehyde, and m-Xylene Oxidation,'' *J. Catal.*, **136**, 554 (1992).

Press, W. H., S. A. Teukolsky, W. T. Vetterling, and B. F. Flannery, *Numerical Recipes in Fortran 77: The Art of Scientific Computing*, 2nd ed., Cambridge University Press, New York, p. 270 (1996).

Raupp, G. B., ''Photocatalytic Oxidation for Point-of-Use Abatement of Volatile Organic Compounds in Microelectronics Manufacturing,'' *J. Vac. Sci. Technol. B*, **13**, 1883 (1995).

Sauer, M. L., and D. F. Ollis, ''Photocatalyzed Oxidation of Ethanol and Acetaldehyde in Humidified Air,'' *J. Catal.*, **158**, 570 (1996).

Spadoni, G., E. Bandini, and F. Santarelli, ''Scattering Effects in Photosensitized Reactions,'' *Chem. Eng. Sci.*, **33**, 517 (1978).

Manuscript received Sept. 8, 1998, and revision received Mar. 10, 1999.